# Large Eddy Simulation of Shock-Boundary Layer Interaction

Susumu Teramoto
*University of Tokyo*
*Hongo 7-3-1, Bunkyo-ku, Tokyo 113-8656, Japan*
*teramoto@thermo.t.u-tokyo.ac.jp*

**Keywords: Boundary layer, Transition, Numerical Simulation**

## Abstract

Large-Eddy Simulation (LES) is applied for the simulation of compressible flat plate boundary with Reynolds number up to $5 \times 10^5$. Numerical examples include shock/boundary layer interaction and boundary layer transition, aiming future application to the analysis of transonic fan/compressor cascades. The present LES code uses hybrid compact/WENO scheme for the spatial discretization and compact diagonalized implicit scheme for the time integration. The present code successfully predicted the bypass transition of subsonic boundary layer. As for supersonic turbulent boundary layer, mean and fluctuation velocity of the attached boundary, as well as the evolution of the friction coefficient and the displacement thickness both upstream and downstream of the separation region are all in good agreement with experiment. The separation point also agreed with the experiment. In the simulation of the shock/laminar boundary layer interaction, the dependence of the transition upon the shock strength is reproduced qualitatively, but the extent of the separation region is overpredicted. These numerical examples show that LES can predict the behavior of boundary layer including transition and shock interaction, which are hardly managed by the conventional Reynolds-averaged Navier-Stokes approach, although there needs to be more effort before achieving quantitative agreement.

## Introduction

The tip speed of front stage of modern axial fan and compressor reaches 450~500 m/s, and relative inlet Mach number exceeds 1.3. The boundary layer over the blade surface interact with shock waves, and therefore Shock/Boundary-Layer Interaction (SLBI) is a key issue at the design of the cascades. In most cases, transonic cascades are designed under the assumption that the boundary layer is fully turbulent. However, chord Reynolds number decreases down to $O(10^5)$ and large part of the boundary layer becomes laminar at high altitude above 100,000ft. Therefore, the prediction of the transition of boundary layer that interact with shock wave, is essential for the design and analysis of fan/compressor operate at low Reynolds number environment.

Numerical simulation based on Reynolds averaged Navier-Stokes (RANS) requires "transition model" to simulate such flowfield. However, there is no reliable transition model applicable to the transition induced by shock/boundary layer interaction.

Recently, direct numerical simulation (DNS) and large eddy simulation (LES) are successfully applied to flowfields including shock/boundary layer interaction,[1)-3)] and boundary layer transition[4)-7)] Although it is still numerically expensive, large eddy simulation is gradually becoming a practical tool rather than a subject of academic research.

In this report, compressible large-eddy simulation is applied to the simulation of flat plate boundary layer with transition and shock wave interaction, and the feasibility of the LES approach to the application to practical transonic cascade is discussed.

## Numerical Methods

### Governing Equations

The governing equations are the spatially filtered three-dimensional Navier-Stokes equations. The formulation of the equations used in this study follows the work of Garnier and Sagaut.[3)]

$$\frac{\partial \bar{\rho}}{\partial t} + \frac{\partial \bar{\rho}\tilde{u}_j}{\partial x_j} = 0$$

$$\frac{\partial \bar{\rho}\tilde{u}_i}{\partial t} + \frac{\partial}{\partial x_j}\bar{\rho}\tilde{u}_i\tilde{u}_j + \frac{\partial \bar{p}}{\partial x_i} = \frac{\partial \check{\sigma}_{ij}}{\partial x_j} - \frac{\partial}{\partial x_j}\tau_{ij}$$

$$\frac{\partial \check{E}}{\partial t} + \frac{\partial}{\partial x_j}\left[\left(\check{E} + \bar{p}\right)\tilde{u}_j\right] = \frac{\partial}{\partial x_j}\left(\check{\sigma}_{ij}\tilde{u}_i\right) - \frac{\partial \check{q}_j}{\partial x_j} - \frac{1}{\gamma - 1}\frac{\partial}{\partial x_j}\left(\overline{pu_j} - \bar{p}\tilde{u}_j\right) - \frac{\partial}{\partial x_j}\left(\tau_{kj}\tilde{u}_k\right) + \tau_{kj}\frac{\partial}{\partial x_j}\tilde{u}_k$$

$$\check{E} = \frac{1}{\gamma - 1}\bar{p} + \frac{1}{2}\bar{\rho}\tilde{u}_i\tilde{u}_j$$

Here, $\bar{}$ and $\tilde{}$ mean filtered and Favre averaged properties respectively. $\check{\sigma}_{ij}$ and $\check{q}_j$ are the resolved stress tensor and heat flux and given as follows

$$\check{\sigma}_{ij} = \mu\left(\frac{\partial \tilde{u}_i}{\partial x_j} + \frac{\partial \tilde{u}_j}{\partial x_i} - \frac{2}{3}\delta_{ij}\frac{\partial \tilde{u}_k}{\partial x_k}\right)$$

$$\breve{q} = \frac{\gamma R}{(\gamma-1)Pr}\mu\frac{\partial \tilde{T}}{\partial x_j}$$

SGS stress tensor $\tau_{ij}$ and the third, forth and fifth terms of the right hand side of the energy equation are modeled using SGS viscosity $\nu_t$

$$\tau_{ij} - \frac{1}{3}\delta_{ij}\tau_{kk} = -\bar{\rho}\nu_t\left(\frac{\partial \tilde{u}_i}{\partial x_j} + \frac{\partial \tilde{u}_j}{\partial x_i} - \frac{2}{3}\delta_{ij}\frac{\partial \tilde{u}_k}{\partial x_k}\right)$$

$$-\frac{1}{\gamma-1}\frac{\partial}{\partial x_j}\left(\overline{pu_j} - \bar{p}\tilde{u}_j\right) = \frac{\gamma R}{(\gamma-1)Pr_t}\bar{\rho}\nu_t\frac{\partial \tilde{T}}{\partial x_j}$$

The isotropic term of the SGS tensor and the pressure-velocity correlation term in the energy equation are neglected.

The SGS viscosity $\nu_t$ is evaluated by Selective Mixed Scale Model[8]

$$\nu_t = f_\theta C_m\sqrt{|S|}(q_c^2)^{1/4}\Delta^{3/2}$$

$S$ is the resolved stress tensor and $q_c^2$ is the test field kinetic energy evaluated as $q_c^2 = \frac{1}{2}(\tilde{u}_i - \hat{\tilde{u}}_i)^2$ where $\hat{}$ denotes test filter. $f_\theta$ is the selective function.

$$f_\theta = \begin{cases} 1 & \text{if } \theta \geq \theta_0 \\ \left(\frac{\tan^2(\theta/2)}{\tan^2(\theta_0/2)}\right)^2 & \text{else} \end{cases}$$

where $\theta$ is the angle between local vorticity $\omega$ and the test filtered vorticity $\hat{\omega}$. This model is simple while it does not require ad hoc damping function near the wall, and the SGS viscosity automatically becomes zero at laminar region.

**Spatial Discretization**

First spatial derivative terms appear in the governing equations are evaluated by sixth-order accurate compact difference scheme.[9]

$$\frac{1}{3}\left(\frac{\partial f}{\partial \xi}\right)_{i-1} + \left(\frac{\partial f}{\partial \xi}\right)_i + \frac{1}{3}\left(\frac{\partial f}{\partial \xi}\right)_{i+1} = \frac{14}{9}\frac{f_{i+1}-f_{i-1}}{2} + \frac{1}{9}\frac{f_{i+2}-f_{i-2}}{4}$$

In order to avoid numerical instability, the physical properties are filtered using tenth-order implicit spatial filter[10] once every time step.

The application of compact difference at region near shock leads to unphysical oscillation, and therefore spatial derivative in the convective terms are evaluated by WENO scheme[11] in regions near shock waves. Classical Jameson type shock sensor multiplied with Ducros's sensor function[12]

$$\left|\frac{\bar{p}_{j+1} - 2\bar{p}_j + \bar{p}_{j-1}}{\bar{p}_{j+1} + 2\bar{p}_j + \bar{p}_{j-1}}\right| \frac{(\mathrm{div}\,\tilde{u})^2}{(\mathrm{div}\,\tilde{u})^2 + (\mathrm{rot}\,\tilde{u})^2 + \varepsilon}$$

is used for the detection of shock waves.

The viscous terms are evaluated by successive application of first derivative operator. Stress tensor is first evaluated at each node using fourth-order central difference, and derivative of the stress tensor is evaluated by the same fourth-order central difference scheme to form the viscous flux.

**Time Integration**

Second-order accurate Crank-Nicolson scheme is used for the time integration

$$\frac{Q_j^{n+1} - Q_j^n}{\Delta t} = \frac{1}{2}\left(R(Q_j^{n+1}) + R(Q_j^n)\right)$$

where $Q^n$ and $R(Q^n)$ denote the solution vector and sum of spatial derivative terms in the governing equations evaluated at $n$th time step.

After applying linearization in time and diagonalize the flux Jacobian matrix as $\frac{\partial R}{\partial Q} = T\Lambda T^{-1}$, the above equation leads to[13]

$$T_j^n\left(1 + \frac{1}{2}\Delta t\frac{\partial \Lambda^n}{\partial x}\right){T^{-1}}_j^n\Delta Q_j^n = R(Q_j^n) \qquad (1)$$

When the spatial derivative term in the left hand side of equation (1) is evaluated by fourth-order accurate compact scheme

$$\left(\frac{\partial \Lambda^n}{\partial x}\right)_{j-1} + 4\left(\frac{\partial \Lambda^n}{\partial x}\right)_j + \left(\frac{\partial \Lambda^n}{\partial x}\right)_{j+1} = 3\left(\Lambda_{j+1}^n - \Lambda_{j-1}^n\right)$$

equation (1) gives[14]

$$[I - 3h\Lambda_{j-1}]\,T_{j-1}^{-1}\Delta Q_{j-1}^n + 4T_j^{-1}\Delta Q_j^n + [I + 3h\Lambda_{j+1}]\,T_{j+1}^{-1}\Delta Q_{j+1}^n = T_{j-1}^{-1}R(Q_{j-1}^n) + 4T_j^{-1}R(Q_j^n) + T_{j+1}^{-1}R(Q_{j+1}^n)$$

Note that the above equation requires only one inversion of scalar tridiagonal matrix to evaluate $\Delta Q_j^n$. This scheme is as efficient as Pulliam's second-order accurate diagonalized implicit scheme.

Errors induced by the linearization and the diagonalization are eliminated by the use of Newton subiteration. For the applications in the present study, three subiterations gave two order of reduction of the residual at Courant-Friedrichs-Lewy (CFL) number of 2.

**Inflow turbulent fluctuation**

In LES (and DNS) simulations, numerical results are considerably influenced by the inflow turbulence, and therefore it is important to specify "realistic" turbulence at the inlet boundary. In this study, two types of inlet turbulence are considered.

*Turbulent boundary layer*

In order to impose turbulent boundary layer which has desired thickness and realistic turbulent fluctuation, rescaling method proposed by Lund[15] is used in the present study.

This method requires auxiliary simulation of spatially-developing boundary layer to generate inflow boundary condition. Physical properties at a sampling plane in the auxiliary simulation domain is decomposed into time-averaged component and fluctuation component.

$$u_i(x,y,z,t) = U_i(x,z) + u_i'(x,y,z,t)$$

Each component is rescaled separately to the target boundary layer thickness, and imposed to the inlet boundaries of both auxiliary and main simulation domain.

As recommended by Sagaut and Garnier,[16] mean component $U_i$ is fixed to the profile evaluated from separate temporally-evolving boundary layer simulation, to avoid long-time drifting of free-stream properties.

*Free-stream turbulence*

Isotropic decaying turbulence in a cubic domain is used for the generation of inflow free-stream turbulence. The size of the cubic domain is equal to the width of the main simulation region. The simulation is started from divergence-free velocity field which has slightly higher turbulent intensity than the desired value. The initial density and pressure are assumed to be uniform, and the initial turbulence spectrum is defined as

$$E \propto k^4 \exp\left[-2(k/k_p)^2\right]$$

The simulation is continued until desired turbulent intensity is achieved, and once the desired isotropic turbulence is achieved, the turbulent flowfield is "frozen" in time.

During the computation of the main simulation, the turbulent fluctuation is sampled over a plane that moves within the cubic isotropic turbulent region with the uniform velocity. The sampled turbulent fluctuation is superimposed over the mean (or time-averaged) inlet profile, and then imposed at the inlet boundary of the main simulation region.

**Grid Resolution**

In LES, the large, energy-carrying eddies have to be resolved, and Piomelli recommends[17] the grid resolution of $\Delta x^+ \sim 100$ and $\Delta z^+ \sim 20$ to resolve eddies inside inner layer of wall boundary layer. In the present study, the grid resolution is set to be $\Delta x^+ \sim 50$, $\Delta y^+_{\min} \sim 1$ and $\Delta z^+ \sim 20$, where $x, y, z$ denote streamwise, wall-normal and crossflow directions respectively.

The geometry of grid used in the present study is $601 \times 65 \times 65$ for Case 1, $253 \times 151 \times 55$ for Case 2 and $401 \times 121 \times 65$ for Case 3.

**Implementation**

The code is parallelized using MPI library. Tridiagonal matrixes appear in the compact difference and the implicit time integration scheme are all inverted locally within each zone. At least four grids are overlapped at the zone interfaces, and not only the physical properties $Q$ but also its increment $\Delta Q$ are exchanged at each subiterations to maintain spatial and temporal accuracy.

The computation required approximately $4\mu$sec/step/node on 4 nodes of Fujitsu VPP800 or Hitachi SR8000. Typical computational time was 100 hours for each case.

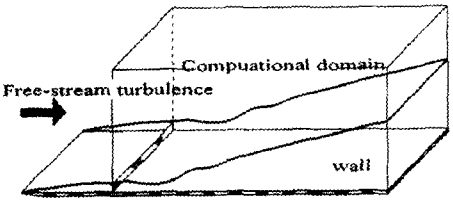


**Fig. 1 Bypass Transition (Case 1)**

## Description of Test Cases

The LES code is applied to the following three flowfield, and the numerical results are compared with experimental data.

**Case 1: Bypass transition of subsonic boundary layer**

When laminar boundary layer is subjected to high free-stream turbulence, initial linear instability stage of the natural transition is bypassed, and turbulent spots are directly produced inside the boundary layer, leading to "bypass transition". Detailed measurement of the bypass transition induced by grid turbulence is reported in the reference,[18] and several researchers reported the results of large-eddy simulation,[19][20]

Figure 1 shows the flowfield considered in this study. The turbulence level is 3%(Case 1A) and 6%(Case 1B) of the free stream velocity. The experiment was carried out at low subsonic (5.3-9.6 m/s), but the uniform flow Mach number is set to be 0.5 in the present numerical simulation to reduce computational time.

**Case 2: Shock/Turbulent boundary layer interaction**

As shown in Fig.2, planer oblique shock wave impinges flat plate turbulent boundary layer. The boundary layer separates upstream of the incident point, and reattaches to form reflected shock wave. The flowfield is symmetric in spanwise direction.

Garnier and Sagaut simulated this flowfield by large-eddy simulation.[3] They compared time-averaged and fluctuation profiles of the boundary layer with experimental data, and showed that their numerical results agree very well with the experiment.

Exactly the same flowfield as Garnier and Sagaut is simulated in this study. The flow parameters are shown in Table. 1.

**Case 3: Shock/Laminar boundary layer interaction**

Flow configuration is same as Case 2, but the inflow boundary layer is laminar. Hakkinen et. al. measured the pitot pressure distribution inside flat plate boundary layer at Mach 2.0, and reduced them to the friction coefficient.[21]

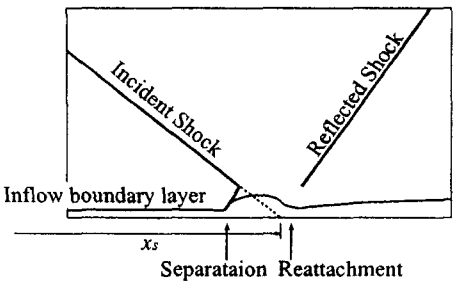


**Fig. 2 Shock/Boundary layer interaction (Case 2 and 3)**

| | |
|---|---|
| Mach Number: | 2.3 |
| Shock incident location: | $x = 336$mm |
| Shock deflection angle: | 8° |
| $\delta_1$ at $x = 260$mm: | 3.535 mm |

**Table 1 Flow parameters (Case 2, Shock / Turbulent boundary layer interaction)[3)]**

| | $Re_s$ | $p_f/p_0$ | Reattachment |
|---|---|---|---|
| Case 3A | $3.96 \times 10^5$ | 1.35 | laminar |
| Case 3B | $4.02 \times 10^5$ | 1.47 | transitional |
| Case 3C | $3.29 \times 10^5$ | 1.91 | turbulent |

**Table 2 Flow parameters (Case 3, Shock / Laminar boundary layer interaction )**

When the pressure ratio is less than 1.35 , boundary layer reattaches as laminar boundary layer, and when the pressure ratio is sufficiently high, the boundary layer reattaches as turbulent boundary layer. And at intermediate pressure ratio, friction at the reattachment point is close to the laminar value, but it gradually increases and reaches to the turbulent value somewhere downstream of the reattachment. The behavior of the boundary layer at the reattachment point is shown in Figure 3. Here, shock pressure ratio $p_f/p_0$ is defined as the ratio between the pressure upstream of the first oblique shock wave and that downstream of the reflected shock wave. Numerical simulation is carried out for three cases shown in Table 2.

The transition of supersonic boundary layer is largely influenced by the acoustic disturbances, but the free stream turbulence intensity of the wind tunnel is not report in the referenced article. In the present simulation, free-stream turbulence of 0.6% of the uniform velocity is imposed at the inlet boundary to break symmetry. The resulting pressure fluctuation upstream of the first incident shock is approximately 3%.

## Results

### Case 1: Bypass transition of subsonic boundary layer

Figure 4 shows the friction coefficients compared with the experimental results.[18)] Numerical simulation for 3% inlet turbulence did not exhibit transition within the computational domain, therefore numerical simulation for 4% inlet turbulence, which results 2.7% freestream turbulence at the middle of the computational domain, is plotted in the figure.

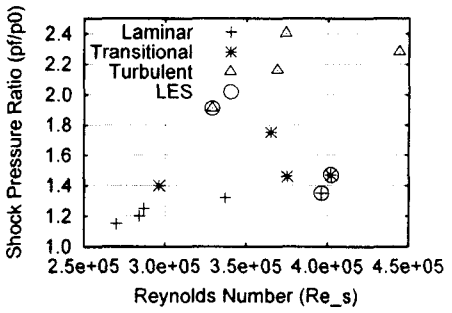


**Fig. 3 Transition of the boundary layer at the reattachment point[21)]**

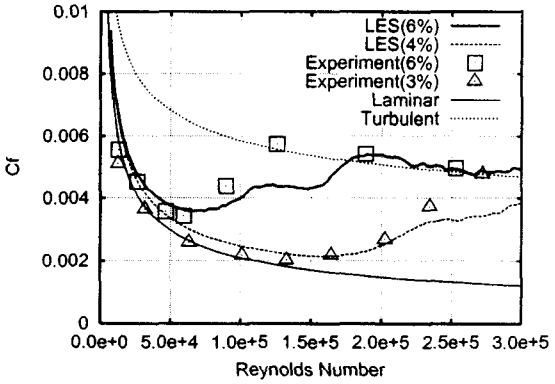


**Fig. 4 Friction coefficient of the boundary layer subjected to free-stream turbulence (Case 1)**

Turbulent transition indicated by the increase in the friction coefficient, is well predicted by the present numerical simulation. (The plateaus observed at the middle of the transition mainly attribute to the insufficient average time (approximately 0.5 wash-out time)) The friction coefficient coincide with the experiment both in the laminar and turbulent regions, and the beginning point of the transition for 6% inlet turbulence agrees well with the experiment. Meanwhile, the numerical simulation predicted the dependence of the transition point upon the turbulence intensity only qualitatively, and slightly higher turbulence intensity (4%) is required to describe the experimental results at 3% turbulence intensity.

### Case 2: Shock/Turbulent boundary layer interaction

Lund's recycling method reasonably predicted both mean velocity and velocity fluctuation at the inlet (Figs.5 and 6). Figure 7 shows the instantaneous shock sensor function value and the

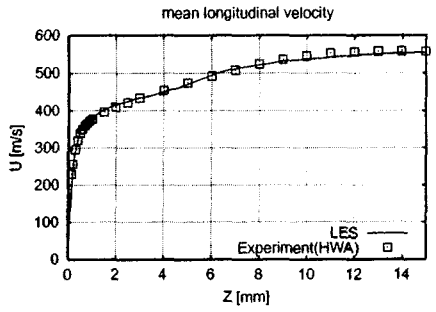


**Fig. 5 Mean velocity profile at the inlet (Case 2)**

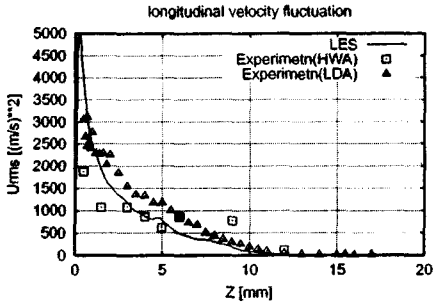


**Fig. 6 Fluctuation velocity profile at the inlet (Case 2)**

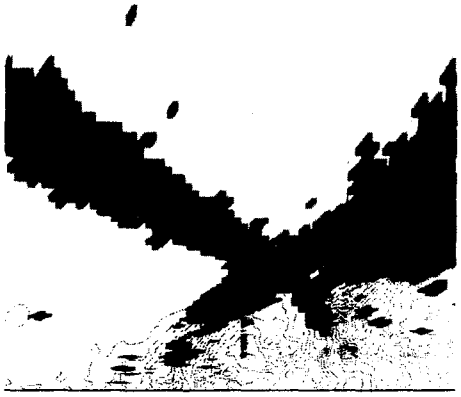

**Fig. 7 Instantaneous shock sensor function value and pressure contour (Case 2)**

pressure distribution. Black region indicate the region where the numerical flux are evaluated by the WENO scheme. The shock sensor function successfully distinguished shock wave from the pressure gradient caused by turbulent fluctuation, and the shock waves are captured without unphysical oscillation.

The present numerical simulation predicted the separated point, which is indicated by sudden decrease in the friction coefficient and the displacement thickness, at $x$ = 300mm. The location is

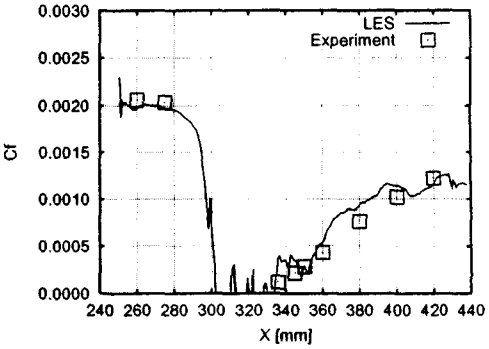


**Fig. 8 Longitudinal evolution of the friction coefficient of the shock/turbulent boundary layer interaction (Case 2)**

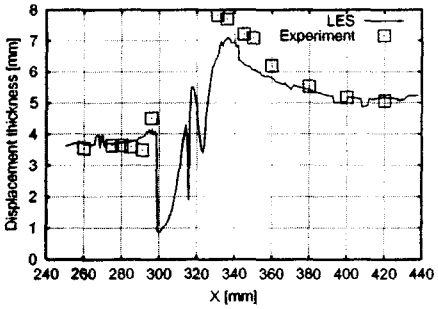


**Fig. 9 Longitudinal evolution of the displacement thickness of the shock/turbulent boundary layer interaction (Case 2)**

approximately 10 mm downstream of the prediction by Garnier and Sagaut.[3] Nevertheless, the evolution of the friction coefficient (Fig.8) and the displacement thickness (Fig.9) are in satisfactory agreement with the experimental results. Garnier and Sagaut commented that the separated zone experimentally measured spreads from $x$ = 300mm and 332mm, and it seems that present computation gives reasonable results concerning the separation zone.

**Case 3: Shock/Laminar boundary layer interaction**

Figures 10(a),(b) show numerical results for Case 3C (turbulent reattachment). The boundary layer separates far upstream of the shock impingement. The separation region is so thin that the compression waves emanate from the leading edge of the separation do not coalesce into shock wave. The incident shock reflects as the expansion fan, and reattachment shock wave is formed behind it. The Reynolds stress starts growing at the shear layer behind the shock impingement. Figure 11 show the averaged velocity distribution at $x$ = 80mm (indicated by gray line in Fig.10(b)). The velocity distribution agrees well with the log-law, and the boundary layer is fully turbulent at

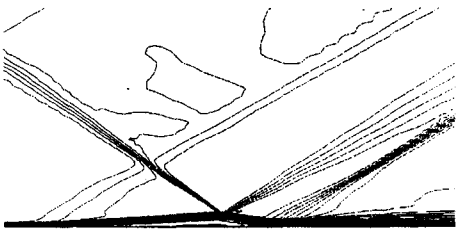

(a) Mach number distribution



(b) Reynolds stress ($u'w'$) distribution

**Fig. 10 Shock/Laminar boundary layer interaction (Case 3C)**

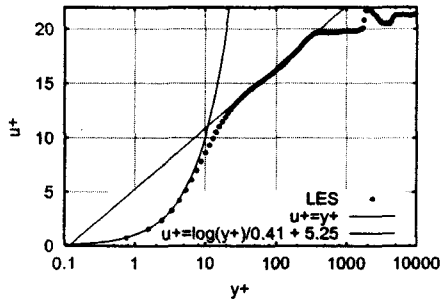


**Fig. 11 Velocity distribution at $x$ = 80mm (Case 3C)**

this location.

Figures 12(a),(b) show the Mach number and Reynolds stress distribution for Case 3A (laminar reattachment). The beginning of the Reynolds stress growth shift downstream of the reattachment, hence the qualitative dependence of the transition upon the shock strength is reproduced by the present numerical simulation.

The quantitative agreement of the friction coefficient is less satisfactory. Figure 13 shows the friction coefficients evaluated from the numerical results. The stronger the shock is, the steeper is the jump in the friction coefficient at the reattachment point. Therefore qualitative dependence of the transition point on the shock strength is also reflected to the friction coefficient. However, the extent of the separation regions are overpredicted in the cases A and B. It is unaccountable that the separation point does not agree with the experiment, since the separation point is completely laminar and finite difference approximation of the Navier-Stokes equations are considered to be quite accurate in this region. In addition, the onset of

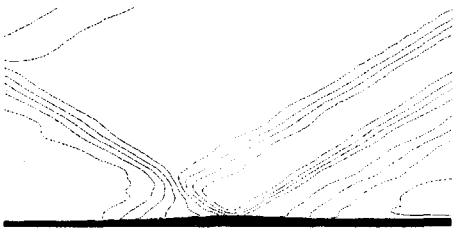

(a) Mach number distribution



(b) Reynolds stress ($u'w'$) distribution

**Fig. 12 Shock/Laminar boundary layer interaction (Case 3A)**

the transition is too early and too steep in these two cases.

The cause of these discrepancy is unknown, but the influence of the inlet turbulent intensity and the wall boundary condition should be investigated in the future studies.

## Conclusions

Large eddy simulation is applied to compressible flat plate boundary layer with shock/boundary layer interaction and transition.

The present code predicted the bypass-transition of the subsonic boundary layer and the shock/turbulent boundary layer interaction very well. Nevertheless, the agreement of the friction coefficient for the transition of the boundary layer induced by the shock impingement is not satisfactory, although qualitative dependence of the transition upon the shock strength is successfully reproduced by the simulation.

The numerical examples show that LES can predict the behavior of boundary layer including transition and shock interaction, which are hardly managed by the conventional Reynolds-averaged Navier-Stokes approach, although there needs to be more effort before achieving quantitative agreement.

## Acknowledgment

This research was financially supported by the Ministry of Education, Culture, Sports, Science and Technology Grant-in-Aid for Young Scientists (B) 14740719, 2003, and part of the numerical simulations were carried out on VPP800 at ISAS/JAXA through the joint research with Center for Planning and Information Systems ISAS/JAXA. The author is grateful to Dr. Eric

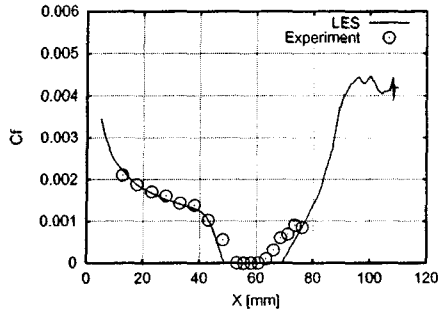


(a) Case 3A ($p_f/p_0 = 1.35$)

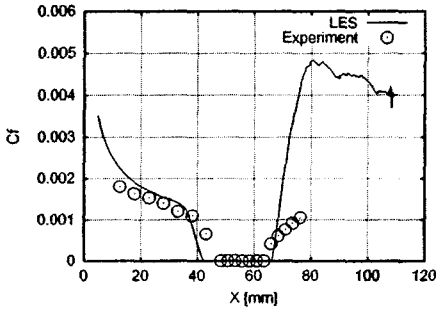


(b) Case 3B ($p_f/p_0 = 1.37$)

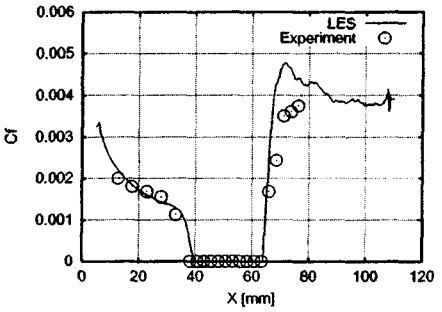


(Cn) Case 3C ($p_f/p_0 = 1.91$)

**Fig. 13 Friction coefficient of shock/Laminar boundary layer interaction (Case 3)**

Garnier for useful discussions and also for providing experimental data.

## References

[1]Sandham, N. D., Yao, Y. F., and Lawal, A. A., "Large-eddy simulation of transonic turbulent flow over a bump," *International Journal of Heat and Fluid Flow*, Vol. 24, 2003, pp. 584–595.

[2]Rizzetta, D. P. and Visbal, M. R., "Application of Large-Eddy Simulation of Supersonic Compression Ramps," *AIAA Journal*, Vol. 40, No. 8, 2002, pp. 1574–1581.

[3]Garnier, E. and Sagaut, P., "Large Eddy Simulation of Shock/Boundary-Layer Interaction," *AIAA Journal*, Vol. 40, No. 10, 2002, pp. 1935–1944, Experimental data was provided through private communication.

[4]Wu, X. H., Jacobs, R. G., Hunt, J. C. R., and Durbin, P. A., "Simulation of boundary layer transition induced by periodically passing wakes," *Journal of Fluid Mechanics*, Vol. 398, 1999, pp. 109–153.

[5]Huai, X., Joslin, R. D., and Piomelli, U., "Large-Eddy Simulation of Transition to Turbulence in Boundary Layers," *Theoretical and Computational Fluid Dynamics*, Vol. 9, No. 2, 1997, pp. 149–163.

[6]Dimas, A. A., Mowli, B. M., and Piomelli, U., "Large-eddy simulation of subcritical transition in an attachment-line boundary layer," *Computers & Mathematics with Applications*, Vol. 46, No. 4, 2003, pp. 571–589.

[7]Matsuura, K., Kato, C., and Yoshiiki, H., "Large Eddy Simulation of Compressible Transitional Cascade Flows," *Proceedings of 17th CFD Symposium*, December 2003, (in Japanese).

[8]Lenormand, E., Sagaut, P., and Phuoc, L. T., "Large Eddy Simulation of Subsonic and Supersonic Channel Flow at Moderate Reynolds Number," *International Journal for Numerical Methods in Fluids*, Vol. 32, 2000, pp. 369–406.

[9]Lele, S. K., "Compact Finite Difference Schemes with Spectral-like Resolution," *Journal of Computational Physics*, Vol. 103, 1992, pp. 16–42.

[10]Gaitonde, D. V. and Visbal, M. R., "Padé-Type Higher-Order Boundary Filters for the Navier-Stokes Equations," *AIAA Journal*, Vol. 38, 2000, pp. 2103–2112.

[11]Jiang, G.-S. and Shu, C.-W., "Efficient Implementation of Weighted ENO Schemes," *Journal of Computational Physics*, Vol. 126, 1996, pp. 202–228.

[12]Ducros, F., Ferrand, V., Nicoud, F., Weber, C., Darracq, D., Gacherieu, C., and Poinsot, T., "Large-Eddy Simulation of the Shock/Turbulence Interaction," *Journal of Computational Physics*, Vol. 152. 1999, pp. 517–549.

[13]Pulliam, T. H., "A Diagonal Form of an Implicit Approximate-Factorization Algorithm," *Journal of Computational Physics*, Vol. 39, 1981, pp. 347–363.

[14]Ekaterinaris, J. A., "Implicit, High-Resolution, Compact Schemes for Gas Dynamics and Aeroacoustics," *Journal of Computational Physics*, Vol. 156, 1999, pp. 272–299.

[15]Lund, T. S., "Generation of Turbulent Inflow Data for Spatially-Developing Boundary Layer Simulation," *Journal of Computational Physics*, Vol. 140, 1998, pp. 233–258.

[16]Sagaut, P., Garnier, E., Tromeur, E., and Larchevêque, L., "Turbulent Inflow Conditions for LES of Supersonic and Subsonic Wall Bounded Flows," AIAA Paper 2003-0068, Jan. 2003.

[17]Piomelli, U. and Balaras, E., "Wall-Layer Models for Large-Eddy Simulations," *Annual Review of Fluid Mechanics*, Vol. 34, 2002, pp. 349–374.

[18]Roach, P. E. and Brierley, D. H., "The Influence of a Turbulent Free-Stream on Zero Pressure Gradient Transitional Boundary Layer Development Part I: Test Cases T3A and T3B," *Nuerical Simulation of Unsteady Flows and Transition to Turbulence*, edited by O. Poronneau, W. Rodi, I. L. Ryhming, A. M. Savill, and T. V. Truong, 1990, pp. 319 347, Proceedings of the ERCOFTAC Workshop.

[19]Voke, P. R. and Yang, Z., "Numerical Study of Bypass Transition," *Physics of Fluids*, Vol. 7, No. 9, 1995, pp. 2256–2264.

[20]Matsuura, K., Kato, C., Yoshiiki, H., and Nagashima, T., "Large Eddy Simulation of Compressible Transitional Cascade Flows," 生産研究, Vol. 55, No. 1, 2003, pp. 59–67, (in Japanese).

[21]Hakkinen, R. J., Greber, I., Thilling, L., and Aabrbanel, S. S., "The Interaction of an Oblique Shock Wave with a Laminar Boundary Layer," NASA MEMO 2-18-59W, National Aeronautics and Space Administration, 1959.